Supporting Information

Fluorescence Modulation via Photoinduced Spin Crossover Switched Energy Transfer from Fluorophore to Fe^{II} Ions

Jun-Li Wang,[a] Qiang Liu,[a] Yin-Shan Meng,[a] Xin Liu,[a] Hui Zheng,[b] Quan Shi,[b] Chun-Ying Duan,[a] Tao Liu[a]*

Table of Contents

Experimental Section

Materials

All reagents were commercially available and were used without further purification. 4-Amino-3, 5-bis(pyridine-2-yl)–1, 2, 4-triazole (abpt) was synthesized according to a procedure in the literature[1].

Synthesis of (pyrene-1-yl)-N-(3, 5-di(pyridin-2-yl)-4H-1, 2, 4-triazol-4-yl) methanimine (L)

A methanol solution of 1-pyrenecarboxaldehyde (5.0 mmol) and abpt (5.0 mmol) in the presence of several drops of acetic acid was refluxed over 8 h and a yellow precipitate was isolated by filtration and washed thoroughly with methanol. The yield is 76 % based on abpt. Anal. Calc. for $C_{29}H_{18}N_6$: H, 4.03; C, 77.32; N, 18.65. Found: H, 3.92; C, 76.99; N, 18.90. ^{1}H NMR (500 MHz, DMSO-d_6, δ) 10.02 (s, 1H), 8.81 (d, J = 9.3 Hz, 1H), 8.61 (d, J = 4.6 Hz, 2H), 8.55 (d, J = 8.1 Hz, 1H), 8.47–8.34 (m, 5H), 8.29 (d, J = 8.9 Hz, 1H), 8.24 (d, J = 7.9 Hz, 2H), 8.18 (t, J = 7.6 Hz, 1H), 8.06 (td, J = 7.8, 1.6 Hz, 2H), 7.52 (dd, J = 7.1, 5.2 Hz, 2H).

Synthesis of $[Fe(L)_2(NCS)_2]$ (1)

A methanol solution of $Fe(NCS)_2$ (0.1 mmol) in the presence of a small quantity of ascorbic acid was added to a DMF solution of L (0.2 mmol). The resulting limpid mixture was stirred for 1 h and then left in diethyl ether vapor. The green crystals were obtained after several weeks. The yield is 35 % based on $Fe(NCS)_2$. Anal. Calc. for $C_{60}H_{36}FeN_{14}S_2$: H, 3.38; C, 67.16; N, 18.28. Found: H, 3.72; C, 66.76; N, 17.87.

Thermogravimetric analyses

Thermogravimetric analysis (TGA) was performed at a rate of 10 °C·min^{-1} under an Ar atmosphere using a TG/DTA Q600 system.

Raman spectroscopy

Raman spectra were obtained using a Raman microscope (LabRAM HR Evolution). The excitation source was a He–Ne laser (632.8 nm, 15 mW; red light source). Variable-temperature Raman data were collected using a Linkam THMS600 liquid nitrogen cryostat with a temperature controller between −196 and 600 °C.

Infrared Spectra

The temperature dependence of infrared spectra was measured on KBr pellet samples using a Nicolet iS10 FT-IR spectrometer equipped with a liquid helium type cryostat (OptistatCF2). The cooling and heating rates are 3 K·min^{-1}. For infrared spectra after irradiation, the sample was irradiated via a flexible optical fiber guided a laser diode pumped Nd:YVO_4 laser (λ = 671 nm) at 20 K.

Powder X-ray diffraction

Powder X-ray diffraction (PXRD) was performed using a Rigaku D/Max 2400 automatic powder X-ray diffractometer with Cu-Kα radiation (λ = 1.5418 Å) at room temperature.

Magnetic and photomagnetic studies

Magnetic susceptibility measurements of samples were performed using a Quantum Design SQUID (MPMS XL-7) magnetometer. Data were corrected for the diamagnetic contribution calculated from Pascal constants. Magnetic studies of the samples were performed under a 1,000 Oe field in the temperature range from 2 K to 400 K at ±1 K min^{-1}. Photoirradiation of the powder samples (m = 0.760 mg) was performed at 10 K with a laser diode pumped Nd:YVO_4 laser (λ = 671 nm)[2]. Temperature-dependent magnetization was measured both before and after irradiation in the temperature range from 2 to 150 K. Difference in the magnetization before and after irradiation was extracted by subtracting the magnetization value before irradiation from that after irradiation. Furthermore, from these magnetization values and the sample weight, differences in the χT values before and after irradiation ($\Delta\chi T$) were calculated.

Heat-capacity measurements

Heat-capacity measurements were performed in zero magnetic field and in the temperature range 2–398 K, using the heat-capacity option of a Quantum Design physical property measurement

system (PPMS). The temperature intervals adopt logarithmic spacing below 100 K and 10 K temperature interval was used in both temperature regions of 100–200 K. The smaller intervals (0.1 K) were used in the transition-temperature region. The sample for the PPMS was prepared as powder, and the accuracy of the heat-capacity measurements on copper and powdered benzoic acid samples was found to be ±1% from T = (22 to 300) K and ±(2 to 5)% below 22 K[3]. The accuracy of the heat-capacity measurements for compound **1** was determined to be ±0.28% and ±0.63% in the temperature ranges 2–10 K and 178–332 K, respectively. The details of the sample preparation and the heat capacity experimental procedure can be found in the corresponding literature reported by Shi et al [4, 5]. The mass of the sample used in this measurement is 8.66 mg.

Fluorescence spectroscopy

Emission spectra of the fluorescence of solid samples were obtained using an Edinburgh FL 900 fluorescence spectrophotometer coupled with a liquid helium type refrigerator (Optistat CF2) with solid sample holder. For the fluorescence emission spectrum after irradiation, the sample was irradiated via a flexible optical fibre guided laser diode pumped Nd:YVO_4 laser (λ = 671 nm) at 10 K.

Ultraviolet–visible spectroscopy

Variable-temperature UV-vis spectra of solid samples were obtained using an Agilent cary5000 spectrophotometer coupled with a Linkam THMS600 liquid nitrogen cryostat with a temperature controller.

Theoretical Methods

Extensive Density Functional Theory/Time-dependent Functional Theory (DFT/ TD-DFT) was performed based on calculations to investigate the photophysics of spin crossover compounds assembled with Fe^{II} ions and (pyrene-1-yl)-N-(3,5-bi(pyridine-2-yl)-4H-1,2,4-triazol-4-yl) methanimine. After extensive benchmark calculations with various basis sets and density functional, all the calculations were performed with PBE0[6] functional in combination with 6-31G(d)[7-9] and Lanl2dz [10, 11] basis sets as implemented in Gaussian 09[12]. The structures of ground states and low-lying excited states of high-spin and low-spin of Fe^{II} complexes were fully optimized and verified with frequency calculations.

The selected structure parameters of the complexes obtained with PBE0 functional and 6-31g(d)/Lanl2dz basis sets were compared with the experimental data in Table S6. The coordination around Fe^{II} ion is a slightly distorted octahedral contributed by N atoms from ligands. The calculated LS and HS ground state structures of the Fe^{II} complex compare well with the experimental counterparts. We plotted the isosurface plot of spin density of Fe^{II}_{HS} complex and found the spin is mainly localized on the Fe^{II}.

Structure Determinations and Refinements

Single-crystal X-ray diffraction data were collected at 277 K and 90 K using the SMART and SAINT programs on a Bruker Smart APEX II–CCD X-ray diffractometer equipped with a graphite-monochromated Mo-Kα radiation source (λ = 0.71073 Å). The structures were solved using a direct method and refined by full-matrix least-squares on F^2 in the SHELX program with anisotropic thermal parameters for all non-hydrogen atoms. Hydrogen atoms were added geometrically and refined using the riding model. The supplementary crystallographic data used in this study are as follows: CCDC-1447594 (complex **1** at 277 K) and CCDC-1447595 (complex **1** at 90 K). These data can be obtained free of charge from the Cambridge Crystallographic Data Centre via www.ccdc.cam.ac.uk/data_request/cif.

References

1. F. Bentiss, M. Lagrenee, M. Traisnel, B. Mernari, H. Elattari, A simple one step synthesis of new 3,5-disubstituted-4-amino-1,2,4-triazoles. *J. Heterocycl. Chem.* 1999 **36**, 149-152.

2. M. Nihei *et al.*, Controlled intramolecular electron transfers in cyanide-bridged molecular squares by chemical modifications and external stimuli. *J. Am. Chem. Soc.* 2011 **133**, 3592-3600.
3. Q. Shi, C. L. Snow, J. Boerio-Goates, B. F. Woodfield, Accurate heat capacity measurements on powdered samples using a Quantum Design physical property measurement system. *J. Chem. Thermodyn.*. 2010 **42**, 1107-1115.
4. R. Dai, S. Zhang, N. Yin, Z.-C. Tan, Q. Shi, Low-temperature heat capacity and standard thermodynamic functions of beta-D-(-)-arabinose ($C_5H_{10}O_5$). *J. Chem. Thermodyn.* 2016 **92**, 60-65.
5. Q. Shi, J. Boerio-Goates, B. F. Woodfield, An improved technique for accurate heat capacity measurements on powdered samples using a commercial relaxation calorimeter. *J. Chem. Thermodyn.* 2011 **43**, 1263-1269.
6. C. Adamo, V. Barone, Toward reliable density functional methods without adjustable parameters: The PBE0 model. *J. Chem. Phys.* 1999 **110**, 6158-6170.
7. R. C. Binning, L. A. Curtiss, COMPACT CONTRACTED BASIS-SETS FOR 3RD-ROW ATOMS - GA-KR. *J. Comput. Chem*. 1990 **11**, 1206-1216.
8. M. M. Francl *et al.*, Self-consistent molecular orbital methods. XXIII. A polarization-type basis set for second-row elements. *J. Chem. Phys.* 1982 **77**, 3654-3665.
9. V. A. Rassolov, M. A. Ratner, J. A. Pople, P. C. Redfern, L. A. Curtiss, 6-31G*basis set for third-row atoms. *J. Comput. Chem.* 2001 **22**, 976-984.
10. P. J. Hay, W. R. Wadt, Ab initio effective core potentials for molecular calculations. Potentials for the transition metal atoms Sc to Hg. *J. Chem. Phys.* 1985 **82**, 270-283.
11. W. R. Wadt, P. J. Hay, Ab initio effective core potentials for molecular calculations. Potentials for main group elements Na to Bi. *J. Chem. Phys.* 1985 **82**, 284-298.
12. Frisch, M. J.; Trucks, G. W.; Schlegel, H. B.; Scuseria, G. E.; Robb, M. A.; Cheeseman, J. R.; Scalmani, G.; Barone, V.; Petersson, G. A.; Nakatsuji, H.; Li, X.; Caricato, M.; Marenich, A. V.; Bloino, J.; Janesko, B. G.; Gomperts, R.; Mennucci, B.; Hratchian, H. P.; Ortiz, J. V.; Izmaylov, A. F.; Sonnenberg, J. L.; Williams; Ding, F.; Lipparini, F.; Egidi, F.; Goings, J.; Peng, B.; Petrone, A.; Henderson, T.; Ranasinghe, D.; Zakrzewski, V. G.; Gao, J.; Rega, N.; Zheng, G.; Liang, W.; Hada, M.; Ehara, M.; Toyota, K.; Fukuda, R.; Hasegawa, J.; Ishida, M.; Nakajima, T.; Honda, Y.; Kitao, O.; Nakai, H.; Vreven, T.; Throssell, K.; Montgomery Jr., J. A.; Peralta, J. E.; Ogliaro, F.; Bearpark, M. J.; Heyd, J. J.; Brothers, E. N.; Kudin, K. N.; Staroverov, V. N.; Keith, T. A.; Kobayashi, R.; Normand, J.; Raghavachari, K.; Rendell, A. P.; Burant, J. C.; Iyengar, S. S.; Tomasi, J.; Cossi, M.; Millam, J. M.; Klene, M.; Adamo, C.; Cammi, R.; Ochterski, J. W.; Martin, R. L.; Morokuma, K.; Farkas, O.; Foresman, J. B.; Fox, D. J. Gaussian 09, Revision D.01 Wallingford, CT, 2016.

Table S1. Crystallographic Data for $[Fe(L)_2(NCS)_2]$ at 277 and 90 K

Temperature, K	**277**	**90**
formula	$C_{60}H_{36}FeN_{14}S_2$	$C_{60}H_{36}FeN_{14}S_2$
Fw	1073.00	1073.00
crystal system	Triclinic	Triclinic
Space group	$P\bar{1}$	$P\bar{1}$
a, Å	8.0020(6)	7.9450(3)
b, Å	9.1057(7)	8.8188(3)
c, Å	17.7358(14)	17.5482(7)
α, °	76.787(4)	77.665(2)
β, °	82.257(4)	82.466(2)
γ, °	80.099(4)	81.092(2)
V, Å^3	1233.20(16)	1180.51(8)
Z	1	1
D_c, g/cm^3	1.445	1.509
μ(Mo K_α), mm^{-1}	0.449	0.469
crystal size, mm^3	0.24×0.22×0.20	0.24×0.22×0.20
θ_{min}, θ_{max} , °	2.32, 25.00	2.38, 24.99
no. total reflns.	23829	22108
no. uniq. reflns (R_{int})	4342 (0.0539)	4148 (0.0447)
no. params	349	349
*R*1,*wR*2 [I≥2σ(I)]	0.0459, 0.0897	0.0345, 0.0794
*R*1,*wR*2 (all data)	0.0798, 0.0976	0.0429, 0.0821
GOF	1.033	1.039

Table S2. Selected bond distances (Å) and angles (°) for $[Fe(L)_2(NCS)_2]$ at 277 K

Bond distances (Å)			
Fe(1)-N(1)	2.077(3)	Fe(1)-N(1A)	2.077(3)
Fe(1)-N(3)	2.1243(19)	Fe(1)-N(3A)	2.1243(19)
Fe(1)-N(2A)	2.197(2)	Fe(1)-N(2)	2.197(2)
Bond angles (°)			
N(1)-Fe(1)-N(1A)	180.00(17)	N(1)-Fe(1)-N(3)	87.71(9)
N(1A)-Fe(1)-N(3)	92.29(9)	N(1)-Fe(1)-N(3A)	92.29(9)
N(1A)-Fe(1)-N(3A)	87.71(9)	N(3)-Fe(1)-N(3A)	180.00(13)
N(1)-Fe(1)-N(2A)	88.94(9)	N(1A)-Fe(1)-N(2A)	91.06(9)
N(3)-Fe(1)-N(2A)	104.55(7)	N(3A)-Fe(1)-N(2A)	75.45(7)
N(1)-Fe(1)-N(2)	91.06(9)	N(1A)-Fe(1)-N(2)	88.94(9)
N(3)-Fe(1)-N(2)	75.45(7)	N(3A)-Fe(1)-N(2)	104.55(7)
N(2A)-Fe(1)-N(2)	180.00(5)		

Symmetry code A: –x + 1, –y, –z.

Table S3. Selected bond distances (Å) and angles (°) for $[Fe(L)_2(NCS)_2]$ at 90 K

Bond distances (Å)			
Fe(1)-N(1A)	1.932(2)	Fe(1)-N(1)	1.932(2)
Fe(1)-N(3)	1.963(2)	Fe(1)-N(3A)	1.963(2)
Fe(1)-N(2A)	2.014(2)	Fe(1)-N(2)	2.014(2)
Bond angles (°)			
N(1A)-Fe(1)-N(1)	180.00(10)	N(1A)-Fe(1)-N(3)	91.95(7)
N(1)-Fe(1)-N(3)	88.05(7)	N(1A)-Fe(1)-N(3A)	88.05(7)
N(1)-Fe(1)-N(3A)	91.95(7)	N(3)-Fe(1)-N(3A)	180.00(11)
N(1A)-Fe(1)-N(2A)	91.13(6)	N(1)-Fe(1)-N(2A)	88.87(6)
N(3)-Fe(1)-N(2A)	99.73(6)	N(3A)-Fe(1)-N(2A)	80.27(6)
N(1A)-Fe(1)-N(2)	88.87(6)	N(1)-Fe(1)-N(2)	91.13(6)
N(3)-Fe(1)-N(2)	80.28(6)	N(3A)-Fe(1)-N(2)	99.73(6)
N(2A)-Fe(1)-N(2)	180.00(5)		

Symmetry code A: –x + 1, –y + 1, –z.

Table S4. Molar heat capacity at constant pressure for **1** from 2 to 400 K measured by PPMS. M = 1073 g·mol^{-1} and experimental pressure p = 0.1 MPa[a, b].

T/K	$C_{p,m}$/(JK^{-1}mol^{-1})	T/K	$C_{p,m}$/(JK^{-1}mol^{-1})	T/K	$C_{p,m}$/(JK^{-1}mol^{-1})	T/K	$C_{p,m}$/(JK^{-1}mol^{-1})
1.9255555	0.391449779	100.76215	396.671965	260.05444	1160.672296	298.38596	1136.185013
2.1401172	0.464598914	110.86958	433.1516366	261.065	1165.156888	299.3745	1134.149325
2.3747498	0.558113105	120.95132	469.1919921	262.07761	1167.290481	301.42564	1136.692061
2.6346239	0.677988903	131.0196	503.5441465	263.06759	1168.4133	302.36517	1145.303895
3.2477978	1.092365694	141.07726	537.7011952	264.14122	1169.721673	307.60026	1143.796589
3.997181	1.866965109	151.19654	572.62174	265.15594	1170.786365	317.60585	1163.67321
4.4341816	2.467413267	161.2944	606.9006487	266.14403	1167.518951	327.74531	1184.921361
4.9204551	3.300016294	171.37415	643.0645879	267.18295	1193.402897	337.84755	1218.608851
5.4598929	4.391761844	181.46399	683.0333991	268.18038	1166.977654	347.93502	1236.221393
6.0553818	5.800321264	191.5428	722.1694111	270.13232	1166.014941	358.01474	1268.671867
6.7188819	7.588290794	201.62478	764.601415	271.14524	1163.69187	368.1013	1306.240588
7.4593242	9.866611661	206.72883	786.1867942	272.1448	1173.088227	378.1575	1337.085344
8.2768427	12.67307756	211.72545	812.4889035	273.16071	1156.764966	388.19379	1369.116267
9.1803145	16.0640184	216.75052	838.1413722	275.15891	1153.139401	398.17559	1401.864389
10.194006	19.99398996	221.81618	874.2343285	276.23928	1148.148426		
11.292598	24.71588522	226.87771	906.2016295	277.37473	1162.448704		
12.530553	30.37464487	231.86089	939.0487639	278.1843	1144.485918		
13.907134	36.98183732	236.9343	974.8209235	279.25691	1143.028973		
15.42773	44.46163972	240.12502	1002.665623	280.26878	1138.894843		
17.122767	53.16818455	241.90076	1026.342471	282.21368	1149.089121		
19.002728	63.16011136	242.03554	1018.655042	282.27839	1137.233375		
21.093286	74.14329293	243.99181	1034.516142	283.29045	1134.629453		
23.407647	86.44693635	244.97766	1046.223597	284.27479	1134.663135		
25.986326	99.87486041	246.01102	1055.681967	285.23508	1134.008311		
28.847429	115.1467464	247.02525	1064.133819	287.29756	1134.009982		
32.02216	131.5443154	248.01851	1072.244989	288.25184	1131.622724		
35.542702	149.4388308	249.0388	1082.275174	290.25848	1131.278556		
39.449775	167.961338	250.04564	1089.985419	291.27908	1131.250391		
43.781018	187.8287846	251.03603	1100.795867	292.28872	1130.206929		
48.581612	208.2399657	252.0262	1116.232081	293.27825	1132.309232		
53.917139	230.8682749	253.06999	1114.965179	294.37493	1130.692876		
59.836455	254.3006216	254.06283	1124.433447	295.37395	1132.238784		
66.409493	279.0780872	255.08389	1131.733422	296.35931	1133.896254		
73.72112	305.1787521	257.0803	1147.199343	297.37282	1133.954572		
81.819893	334.7940119	258.04887	1152.033722				
90.787596	366.2001759	259.05338	1157.014899				

[a] The combined standard uncertainties in the values of the heat capacities are determined to be $\pm 0.03 \cdot C_{p,m}$ for T/K < 20 and $\pm 0.01 \cdot C_{p,m}$ for 20 < T/K < 400.

[b] Standard uncertainties u are $u(T)$ = 0.01 K, $u(p)$ = 2 kPa.

Table S5. Fitting parameters of the Debye and Einstein functions used in the lattice estimation from 2 to 400 K.

Parameters	Complex **1**
m/mol	55.212
Θ_D/K	200.07
n_1/mol	16.870
$\Theta_{E,1}$ /K	1604.3
n_2/mol	28.265
$\Theta_{E,2}$ /K	645.06
%RMS	0.63778

Table S6. Comparison of selected bond length (Å) of experimental data and theoretical calculations.

	Exp.		Thero.	
	LS	HS	LS	HS
Fe-N3(NCS)	1.93	2.08	1.96	2.08
Fe-N4(Py)	2.01	2.20	2.01	2.27
Fe-N5	1.96	2.13	2.00	2.26
Fe-N59	1.93	2.08	1.96	2.08
Fe-N60	2.01	2.20	2.01	2.27
Fe-N61	1.96	2.13	2.00	2.26

Table S7. The predicted excitation energies (E/λ), corresponding oscillator strengths (f) and assignment of the electronic transitions of Fe^{II}_{LS} complex calculated with TD-pbe0 functional at 6-31g(d)//lanl2dz level.

No.	Energy [a]	f [b]	Composition [c]	CI [d]	Character
1	1.8930 eV/654.95 nm	0.0001	265→ 288	0.31320	d→d, L→L’
			270→ 288	0.29330	d→d, L→L’
2	2.0067 eV/617.84 nm	0.0003	271→272	0.66054	L→L’, M→L’
5	2.1284 eV/582.53 nm	0.0003	270→ 272	0.65896	L→L’, M→L’
8	2.2992 eV/539.26 nm	0.0018	271→ 274	0.64559	L→L’, M→L’
10	2.4358 eV/509.01 nm	0.0375	270 → 274	0.64416	L→L’, M→L’
12	2.4929 eV/497.35 nm	0.0004	269 → 273	0.66207	L→L’
15	2.5715 eV/482.15 nm	0.0017	268→ 273	0.64193	L→L’
18	2.8564 eV/434.05 nm	0.0008	269→ 275	0.43981	L→L’
			271→ 276	0.52726	L→L’, M→L’
21	2.9290 eV/423.30 nm	0.0023	269→ 275	0.52425	L→L’
			271→ 276	0.41405	L→L’, M→L’
22	2.9594 eV/418.95 nm	0.0162	268→ 275	0.60041	L→L’
			270→ 276	0.33858	L→L’, M→L’
24	3.0374 eV/408.20 nm	0.0193	268→ 275	0.32453	L→L’
			270→ 276	0.58109	L→L’, M→L’
26	3.1600 eV/392.36 nm	0.9411	266→ 273	0.38439	IL
			267→ 272	0.52200	IL, M→L’
28	3.2336 eV/383.43 nm	0.2202	265→ 272	0.54770	L→L’, M→L’

[a] Only the electronic transitions with excitation energy lower than 380 nm are presented.

[b] Oscillator strength.

[c] Only the main configurations are presented.

[d] The CI coefficients are in absolute values.

Table S8. The predicted excitation energies (E/λ), corresponding oscillator strengths (f) and assignment of the electronic transitions of Fe^{II}_{HS} complex calculated with TD-pbe0 functional at 6-31g(d)//lanl2dz level.

No.	Energy [a]	f [b]	Composition [c]	CI [d]	Character
3	1.6305 eV/760.41 nm	0.0001	265B -> 300B	0.48483	d→d, L→L’
			265B -> 293B	0.39281	L→L’
			268B -> 300B	0.30527	d→d, L→L’
			268B -> 293B	0.24680	L→L’
4	1.7913 eV/692.16 nm	0.0001	268A -> 274A	0.64220	IL
			263B -> 270B	0.63164	L→L’
5	1.7946 eV/690.88 nm	0.0001	269A -> 275A	0.64094	IL
			264B -> 271B	0.63128	IL
6	1.8320 eV/676.79 nm	0.0001	265B -> 288B	0.49342	d→d
			265B -> 290B	0.46607	M→L, L→L’
			268B -> 288B	0.31253	d→d
			268B -> 290B	0.29709	M→L, L→L’
7	2.5175 eV/492.49 nm	0.0016	271A -> 274A	0.45838	L→L’
			273A -> 274A	0.82631	M→L, L→L’
8	2.5388 eV/488.37 nm	0.0015	271A -> 275A	0.49159	L→L’
			273A -> 275A	0.78391	M→L, L→L’
9	2.5460 eV/486.98 nm	0.0006	268B -> 270B	0.48257	L→L’
			269B -> 270B	0.83242	M→L, L→L’
10	2.5570 eV/484.88 nm	0.0013	270A -> 274A	0.44696	L→L’
			272A -> 274A	0.82947	M→L, L→L’
11	2.5715 eV/482.15 nm	0.0006	268B -> 271B	0.71423	M→L, L→L’
			269B -> 271B	0.63879	L→L’
12	2.5828 eV/480.03 nm	0.0012	270A -> 275A	0.51221	L→L’
			271A -> 275A	0.43965	L→L’
			272A -> 275A	0.68290	M→L, L→L’
13	2.6017 eV/476.56 nm	0.0072	266B -> 270B	0.53076	M→L, L→L’
			267B -> 270B	0.75918	L→L’
14	2.6199 eV/473.24 nm	0.0071	266B -> 271B	0.55932	M→L, L→L’
			267B -> 271B	0.75441	L→L’
15	2.7266 eV/454.73 nm	0.0043	265B -> 270B	0.41201	M→L, L→L’

			265B -> 271B	0.33058	M→L, L→L’
			265B -> 273B	0.31592	M→L, L→L’
			268B -> 270B	0.42261	M→L, L→L’
			268B -> 271B	0.30232	M→L, L→L’
			268B -> 273B	0.29426	M→L, L→L’
16	2.7547 eV/450.09 nm	0.0001	265B -> 270B	0.31254	M→L, L→L’
			265B -> 271B	0.35950	M→L, L→L’
			268B -> 270B	0.41237	M→L, L→L’
			268B -> 271B	0.41271	M→L, L→L’
			269B -> 271B	0.40851	L→L’
17	2.8229 eV/439.21 nm	0.0003	271A -> 274A	0.81396	L→L’
			273A -> 274A	0.49778	M→L, L→L’
18	2.8298 eV/438.14 nm	0.0004	271A -> 275A	0.72597	L→L’
			272A -> 275A	0.32230	M→L, L→L’
			273A -> 275A	0.55058	M→L, L→L’
19	2.8561 eV/434.10 nm	0.0008	265B -> 270B	0.37615	M→L, L→L’
			266B -> 270B	0.35411	M→L, L→L’
			268B -> 270B	0.49010	M→L, L→L’
			269B -> 270B	0.31707	L→L’
			269B -> 272B	0.33810	L→L’, L→M
22	2.8842 eV/429.87 nm	0.0001	270A -> 275A	0.76553	L→L’
			272A -> 275A	0.58407	L→L’, L→M
23	2.9101 eV/426.05 nm	0.0117	265B -> 270B	0.43169	M→L, L→L’
			266B -> 270B	0.56847	M→L, L→L’
			267B -> 270B	0.50130	L→L’
24	2.9202 eV/424.57 nm	0.0040	265B -> 271B	0.43546	M→L, L→L’
			266B -> 271B	0.52201	M→L, L→L’
			267B -> 271B	0.48989	L→L’
26	2.9489 eV/420.45 nm	0.0001	273A -> 277A	0.24847	M→L, L→L’

			268B -> 272B	0.63871	IL
			269B -> 273B	0.29241	IL
27	2.9799 eV/416.07 nm	0.0046	273A -> 276A	0.53692	M→L, L→L’
28	3.0005 eV/413.21 nm	0.0002	273A -> 277A	0.59676	M→L, L→L’
			268B -> 272B	0.44265	L→L’
29	3.0176 eV/410.87 nm	0.0061	265B -> 270B	0.27914	M→L, L→L’
			265B -> 273B	0.23835	M→L, L→L’
			266B -> 273B	0.33473	M→L, L→L’
			267B -> 272B	0.46821	M→L, L→L’
			268B -> 273B	0.41704	M→L, L→L’
30	3.0279 eV/409.48 nm	0.0241	271A -> 277A	0.24799	L→L’
			273A -> 276A	0.45587	L→L’
			265B -> 273B	0.35288	M→L, L→L’
			267B -> 272B	0.51756	L→M, L→L’
			268B -> 273B	0.30639	M→L, L→L’
31	3.0497 eV/406.55 nm	0.0010	271A -> 276A	0.34020	L→L’
			272A -> 277A	0.40099	L→L’
			273A -> 277A	0.38365	L→L’
			266B -> 272B	0.53201	M→L, L→L’
			267B -> 273B	0.35897	L→L’
32	3.0619 eV/404.92 nm	0.0026	270A -> 277A	0.33235	L→L’
			272A -> 276A	0.68947	L→L’
33	3.0683 eV/404.08 nm	0.0005	263A -> 274A	0.43728	IL
			268A -> 280A	0.28267	IL
			259B -> 270B	0.46904	IL
			263B -> 276B	0.27777	IL
34	3.0745 eV/403.26 nm	0.0004	270A -> 276A	0.36916	L→L’
			271A -> 276A	0.32800	L→L’
			272A -> 276A	0.28537	M→L, L→L’

			272A -> 277A	0.53958	M→L, L→L’
			266B -> 272B	0.32578	M→L, L→L’
35	3.0781 eV/402.80 nm	0.0005	264A -> 275A	0.41165	IL
			269A -> 281A	0.27393	IL
			260B -> 271B	0.42979	IL
			264B -> 277B	0.27167	IL
37	3.1224 eV/397.08 nm	0.0021	265A -> 277A	0.28385	IL
			273A -> 276A	0.34291	M→L, L→L’
			261B -> 273B	0.26519	IL
			262B -> 272B	0.26159	IL
39	3.1737 eV/390.67 nm	0.0008	265B -> 272B	0.50953	L→L’
			269B -> 273B	0.61632	L→L’
40	3.1945 eV/388.11 nm	1.1074	268A -> 274A	0.49233	IL
			269A -> 275A	0.43316	IL
			263B -> 270B	0.49372	IL
			264B -> 271B	0.43844	IL
41	3.2129 eV/385.90 nm	0.0016	268A -> 274A	0.40960	IL
			269A -> 275A	0.44160	IL
			271A -> 276A	0.32281	L→L’
			263B -> 270B	0.39490	IL
			264B -> 271B	0.42635	IL
42	3.2171 eV/385.39 nm	0.0073	271A -> 276A	0.55332	L→L’
43	3.2280 eV/384.09 nm	0.0087	271A -> 277A	0.67746	L→L’
44	3.2358 eV/383.16 nm	0.0013	265B -> 272B	0.32065	L→L’
			266B -> 272B	0.33328	L→L’
			267B -> 273B	0.55977	L→L’
			268B -> 273B	0.31398	M→L, L→L’
45	3.2419 eV/382.44 nm	0.0079	271A -> 277A	0.35819	L→L’
			265B -> 273B	0.35237	M→L, L→L’

			266B -> 273B	0.31415	M→L, L→L’
			267B -> 273B	0.29010	L→L’
			268B -> 273B	0.46943	M→L, L→L’
46	3.2616 eV/380.14 nm	0.0005	263A -> 274A	0.31635	IL
			259B -> 270B	0.34745	IL
48	3.2804 eV/377.95 nm	0.0008	270A -> 276A	0.65905	L→L’
			270A -> 277A	0.39372	L→L’
			272A -> 276A	0.26276	M→L, L→L’
			272A -> 277A	0.36739	M→L, L→L’
49	3.2859 eV/377.32 nm	0.0008	270A -> 276A	0.37437	L→L’
			265B -> 273B	0.34456	M→L, L→L’
			266B -> 273B	0.58660	M→L, L→L’
50	3.2975 eV/375.99 nm	0.0014	270A -> 276A	0.29289	L→L’
			270A -> 277A	0.74259	L→L’
			272A -> 276A	0.32574	M→L, L→L’
			266B -> 273B	0.23191	M→L, L→L’

[a] Only the electronic transitions with excitation energy lower than 380 nm are presented.

[b] Oscillator strength.

[c] Only the main configurations are presented.

[d] The CI coefficients are in absolute values.

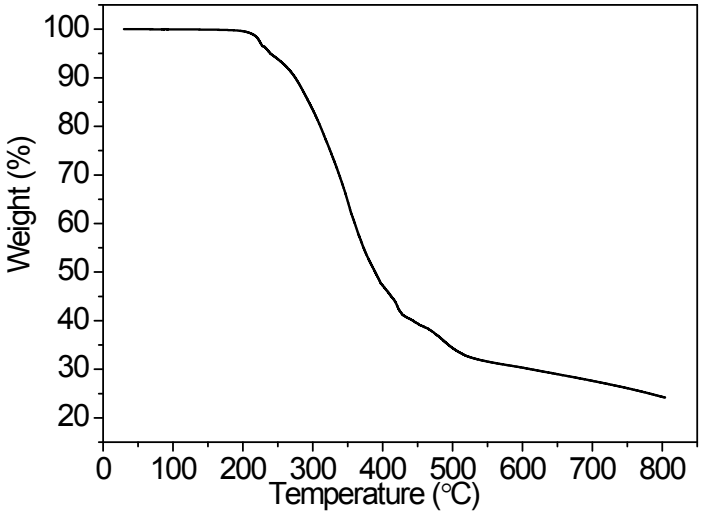

Fig. S1 TGA curve for $[Fe(L)_2(NCS)_2]$ in an Ar atmosphere with a heating rate of 10 °C·min^{-1}.

The complex does not exhibit weight loss below 200 ºC, and then began to decompose rapidly with temperature increased. This confirms that there is no solvent molecule present in the structure, which is in agreement with the crystal structure.

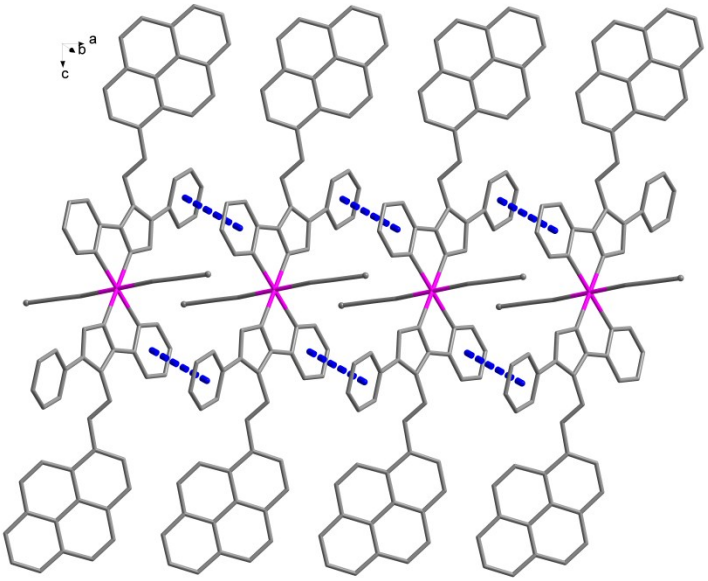

(a)

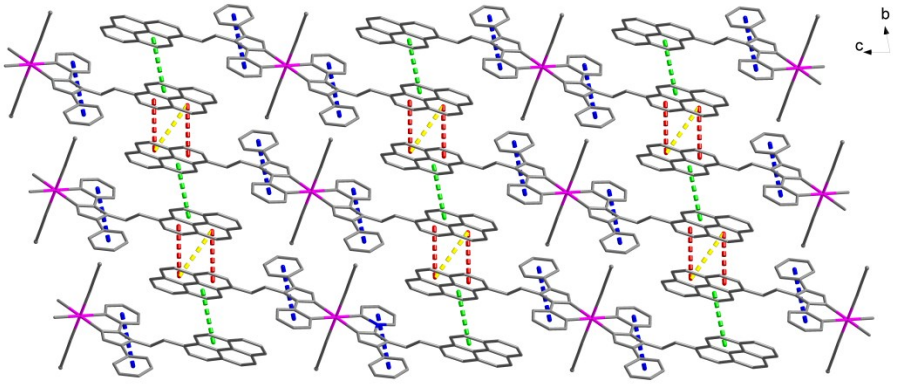

(b)

Fig. S2 (a) 1D chain structure of **1**. The blue dashed line represents the π···π interaction. (b) 3D supermolecular structure of **1**. The dashed lines represent the π···π interaction.

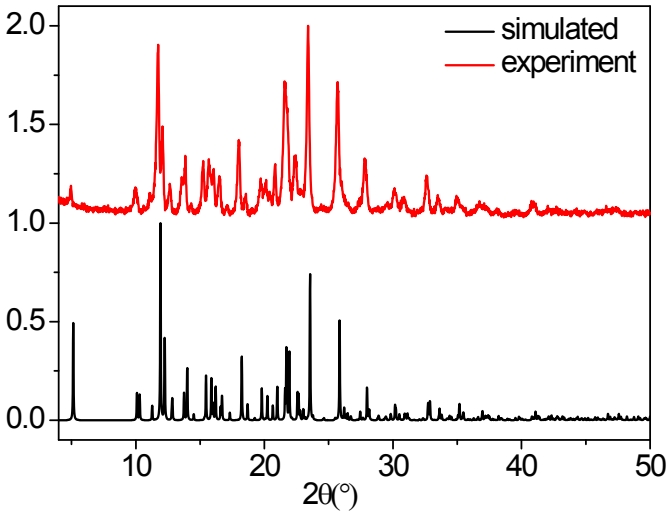

Fig. S3 Powder X-ray diffraction patterns of experiment and simulated from the crystal data for **1**.

Phase purity of **1** was confirmed at ambient conditions by powder X-ray diffraction. The experimental XRPD patterns are consistent with the simulated those as gleaned from the single-crystal X-ray diffraction data.

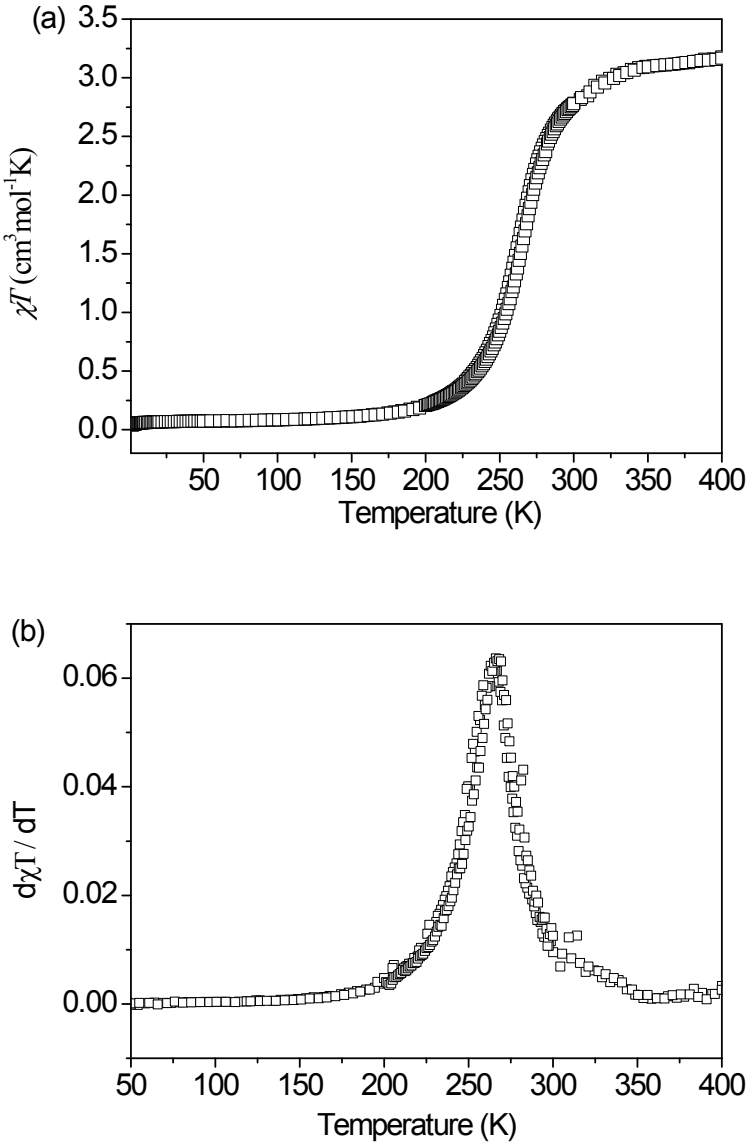

Fig. S4 (a) Temperature dependence of magnetic susceptibilities of **1**. (b) Plot of dχT/dT versus temperature indicating the $T_{1/2}$ value of 267 K at the maximum.

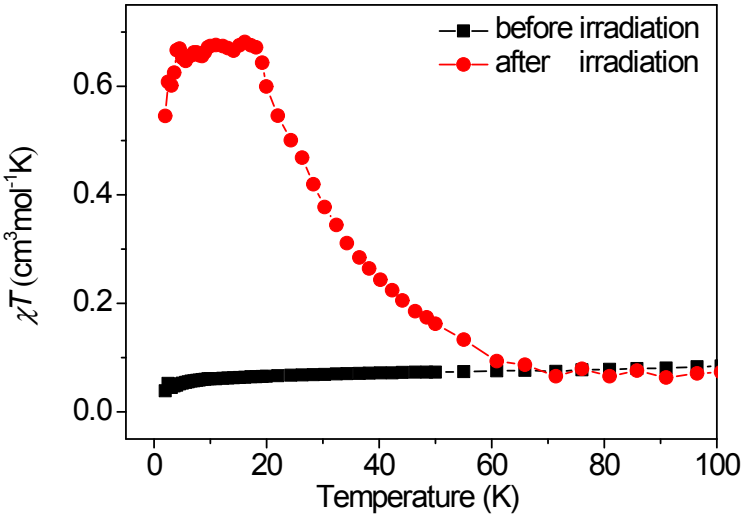

Fig. S5 Temperature dependence of magnetic susceptibilities before and after irradiation for **1**.

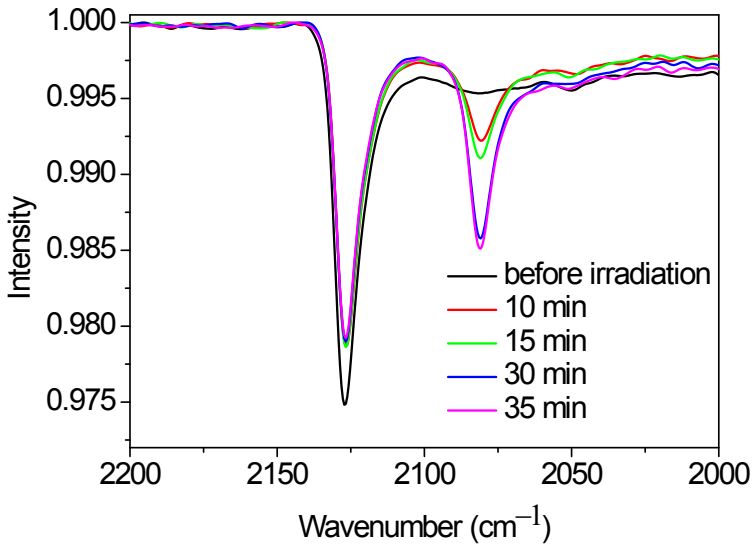

Fig. S6 Irradiation-time dependence of the IR spectra of **1** irradiated at 671 nm at 20 K.

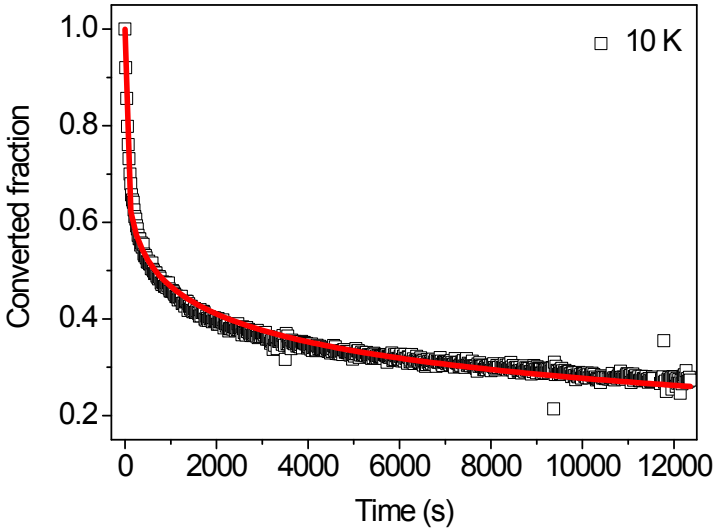

Fig. S7 Relaxation kinetics of the photoinduced fraction for **1** in normalized values (t = 0, converted fraction = 1) at 10 K (black □). The red solid line is the stretched-exponential fit to Equation (1).

Relaxation of the photoinduced metastable state after light irradiation was monitored at 10 K to probe the stability of the photoinduced phases. The decay of magnetization, normalized to the photoinduced fraction γ, was fitted by a stretched exponential law [Eq. (1)]:

$$\gamma(t) = \gamma(0)\exp(-t/\tau)^{\beta} \qquad (1)$$

Where τ represents the relaxation time of the system and β represents the factor of time-evolving magnetic interactions during the decay owing to different magnetic interaction topologies in the high- and low-temperature phases. The best-fit result is $\tau = 3331.75$ s and $\beta = 0.23$. The relatively short time scale of the decay kinetics is responsible for incomplete photoinduced SCO in the system.

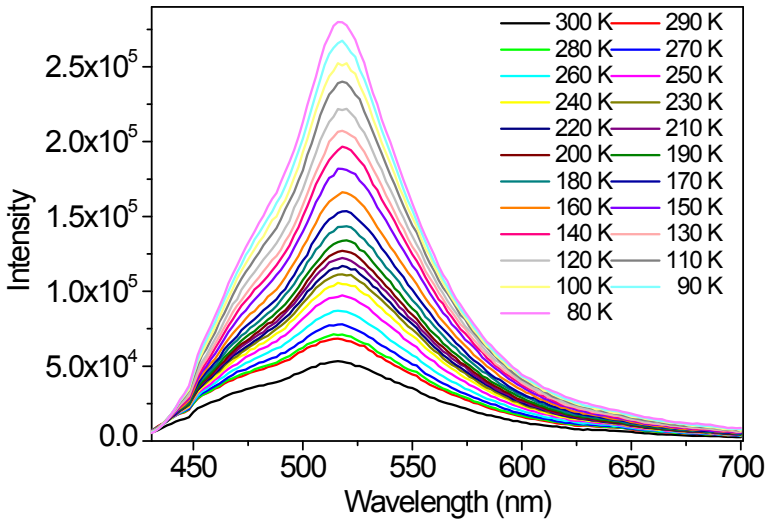

Fig. S8 Temperature-dependent fluorescence emission spectra of ligand.

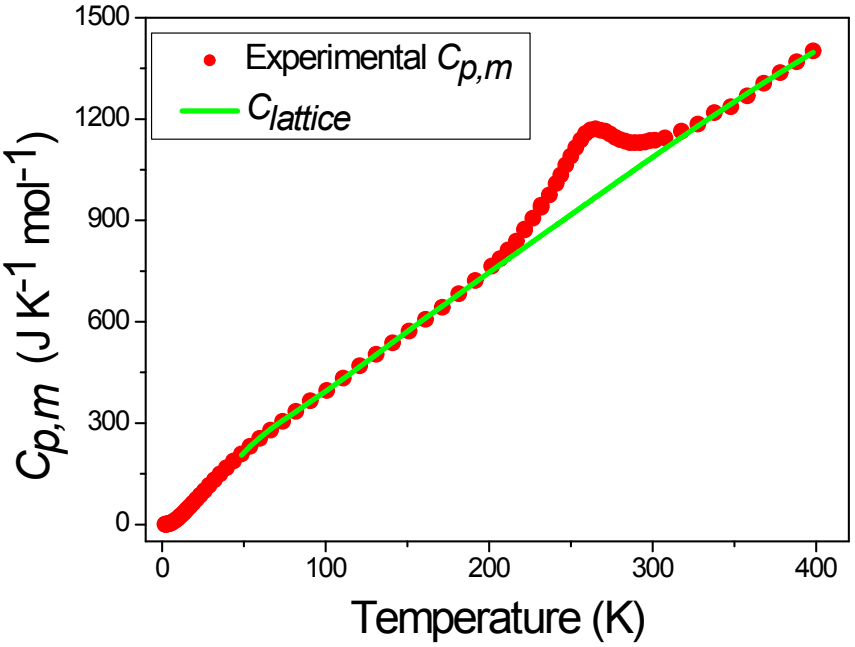

Fig. S9 Temperature dependence of molar heat capacity of **1**. The solid curve shows the estimated lattice heat capacity.

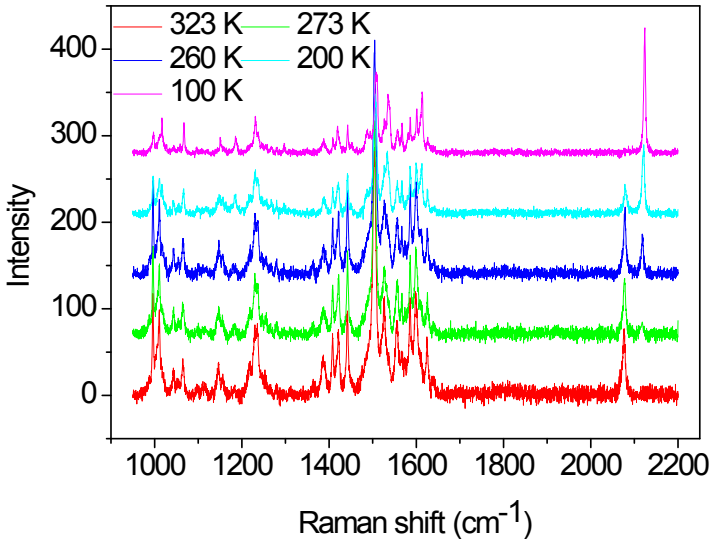

Fig. S10 Raman spectra (λ_{ex} = 633 nm) for **1** at different temperatures.

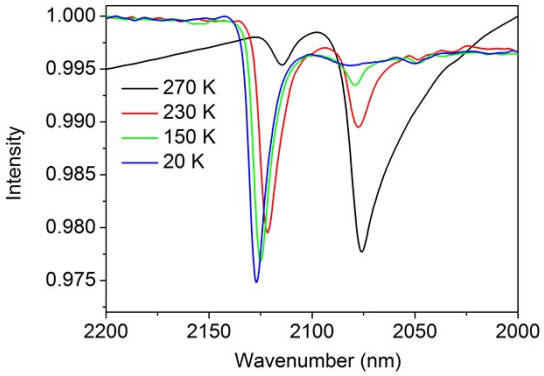

Fig. S11 IR spectra for **1** at different temperatures.

264α

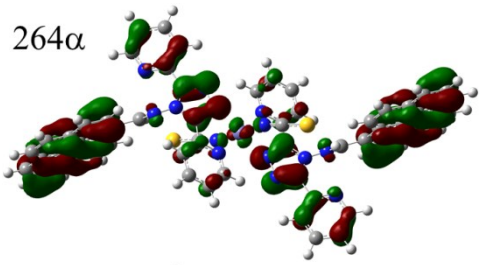

264β

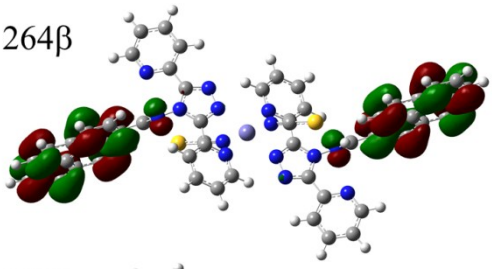

265α

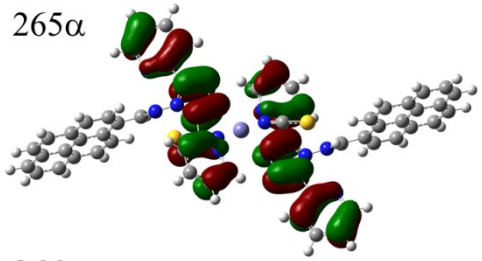

265β

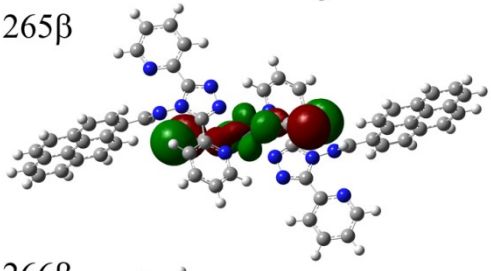

266α

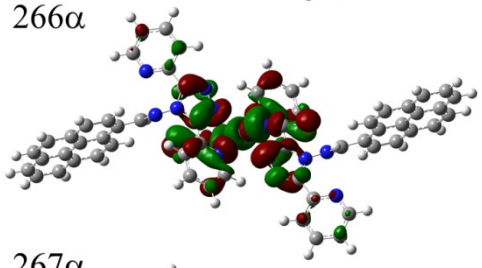

266β

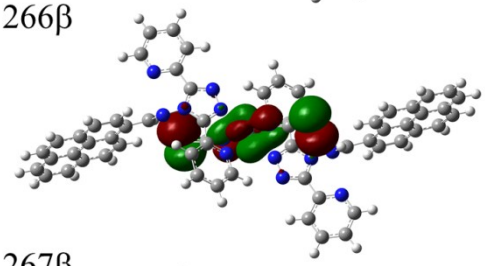

267α

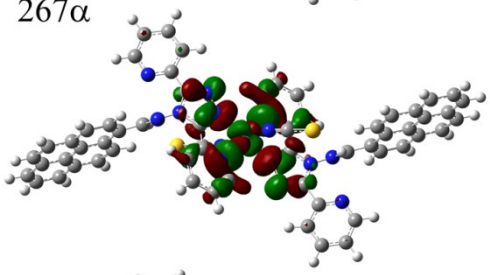

267β

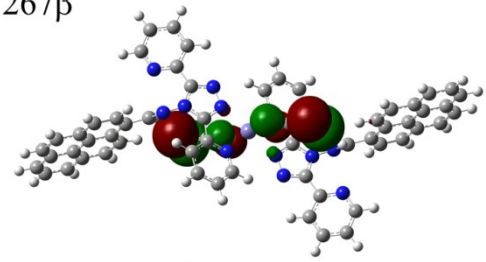

268α

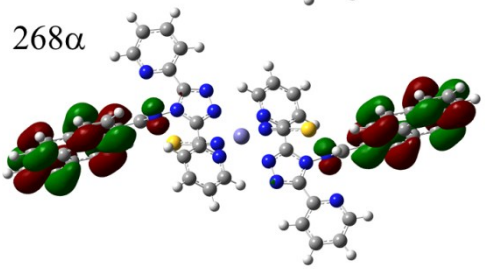

268β

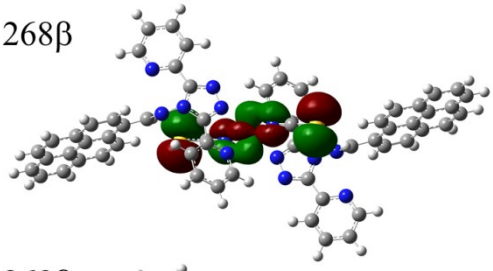

269α

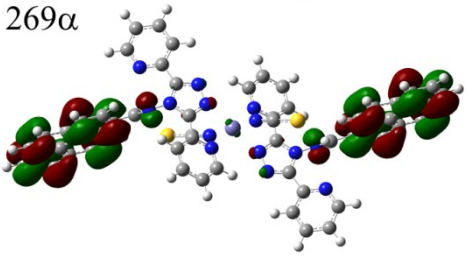

269β

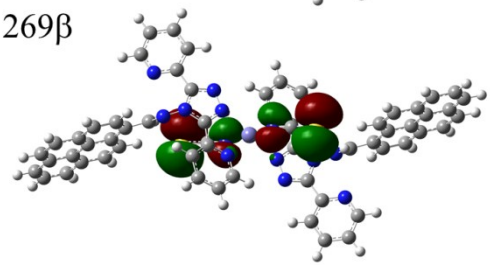

270α

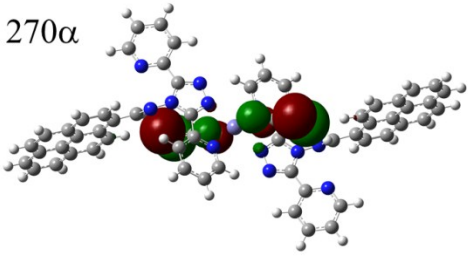

270β

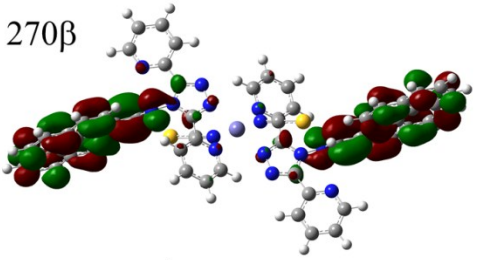

271α

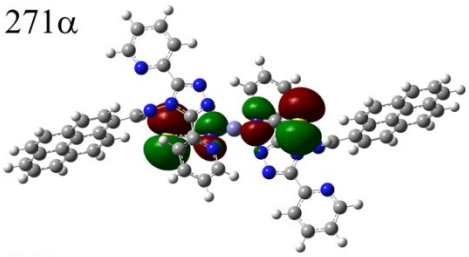

271β

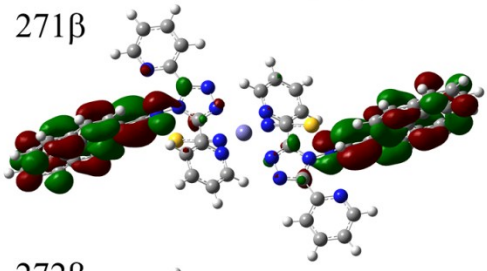

272α

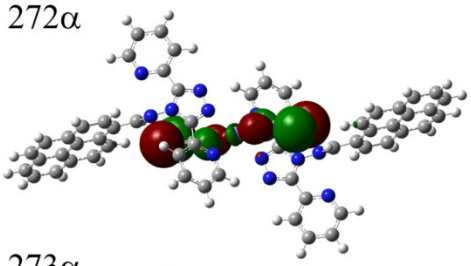

272β

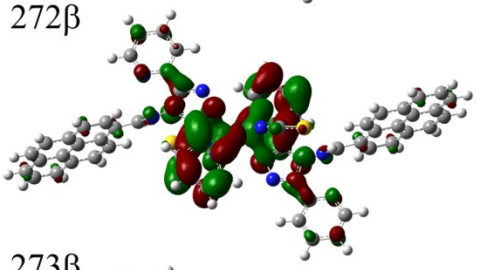

273α

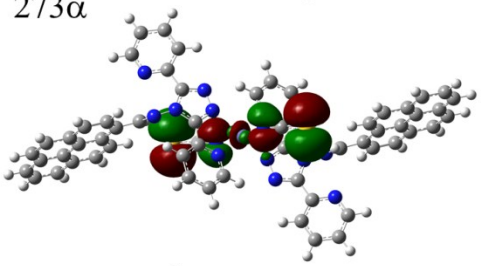

273β

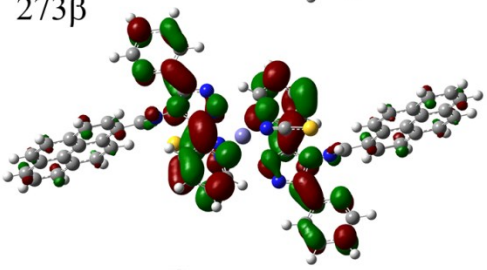

274α

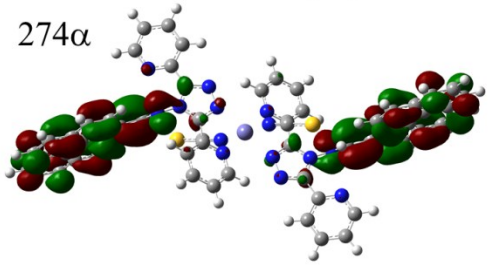

274β

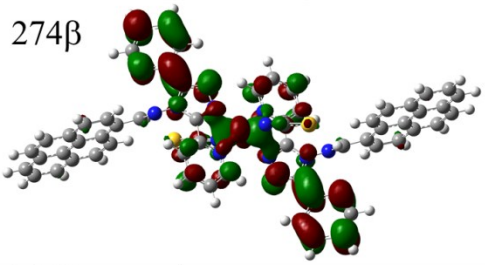

275α

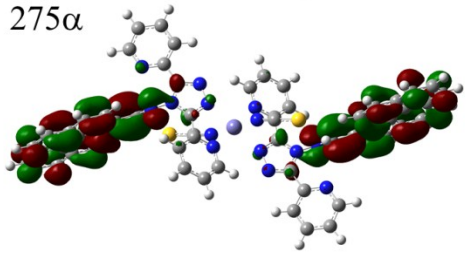

275β

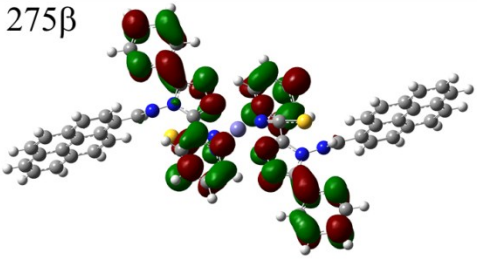

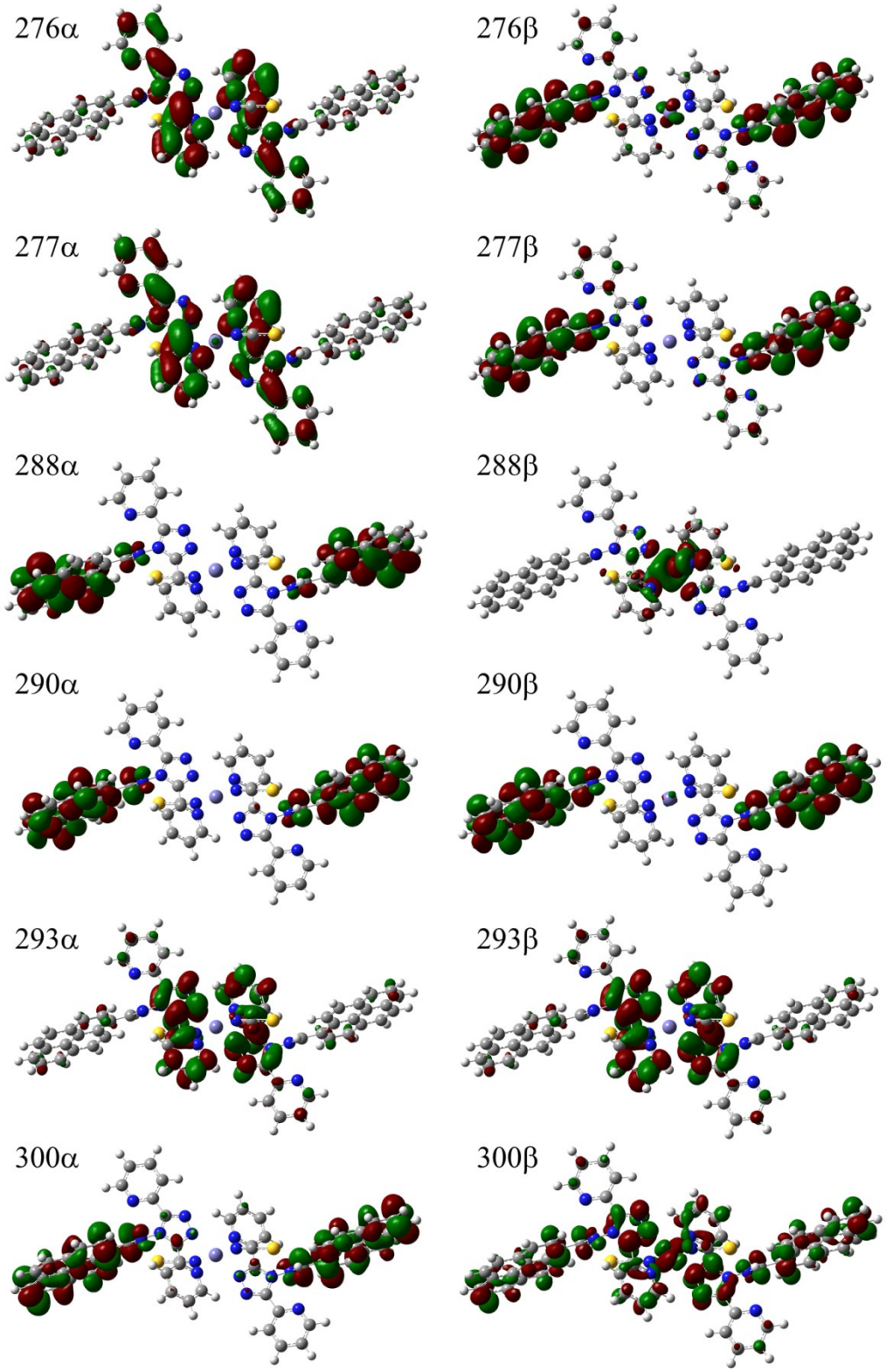

Fig. S12 Isosurface plot of wave function of selected molecular orbitals of Fe^{II}_{HS} complex (isovalue= 0.02 a.u.).

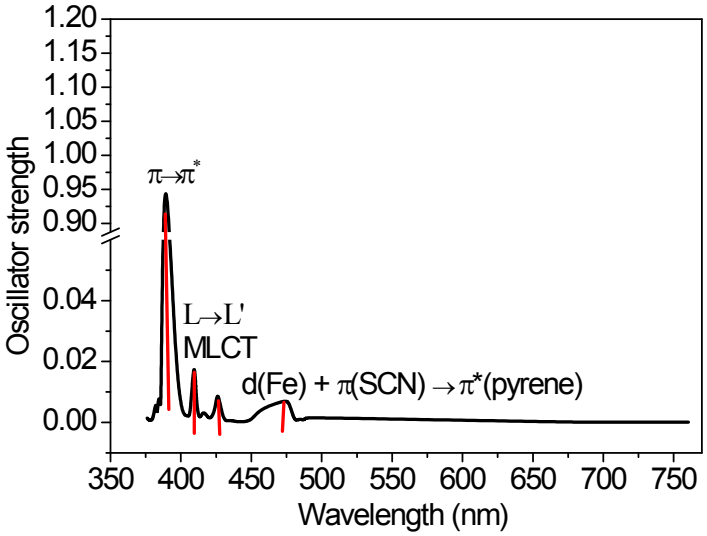

Fig. S13 The TD-DFT calculated UV−Vis spectrum of complex **1** in the HS state.

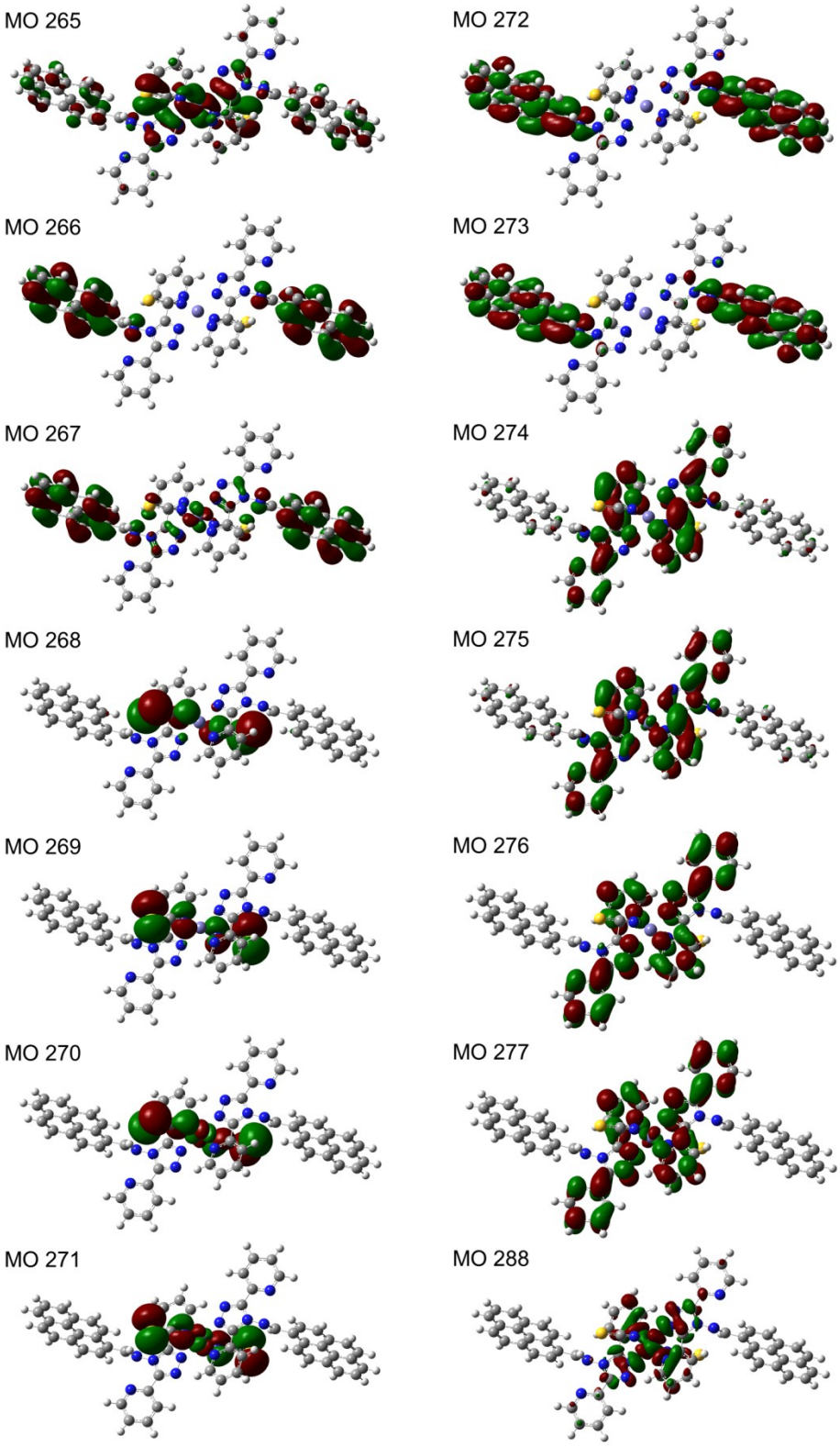

Fig. S14 Isosurface plot of wavefunction of selected molecular orbitals of Fe^{II}_{LS} complex (isovalue= 0.02 a.u.).

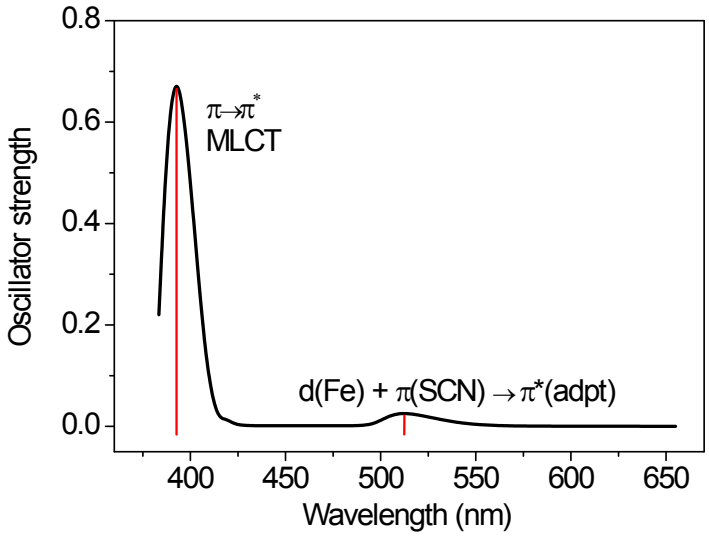

Fig. S15 The TD-DFT calculated UV−Vis spectrum of complex **1** in the LS state.

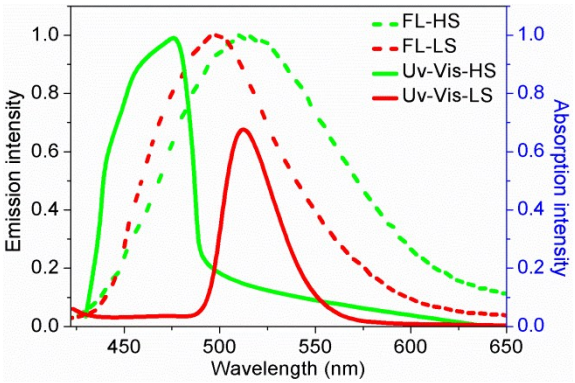

Fig. S16 Normalized fluorescence emission (dash lines) and calculated UV−vis absorption (solid lines) spectra of **1** in the HS state (green lines) and LS state (red lines).